PCCP

RSC Publishing

PAPER

View Article Online
View Journal | View Issue

Cite this: *Phys. Chem. Chem. Phys.*, 2013, **15**, 7277

Vortex domain structures of an epitaxial ferroelectric nanodot and its temperature-misfit strain phase diagram

W. J. Chen,[a] Yue Zheng,*[a] B. Wang,[a] D. C. Ma[b] and F. R. Ling[c]

Received 11th January 2013,
Accepted 12th March 2013

DOI: 10.1039/c3cp00133d

www.rsc.org/pccp

Phase field simulations were conducted to investigate the effect of misfit strain on the vortex domain structure (VDS) in a $BaTiO_3$ nanodot. Taking into account the effect of inhomogeneous eletromechanical fields, ambient temperature and surface effects, our calculations demonstrate a strong effect of misfit strain on the orientation and magnitude of the polarization dipoles. As a consequence, fruitful equilibrium vortex domain patterns can be obtained by adjusting the epitaxial misfit strain between the substrate and the nanodot. While the nanodot exhibits a single transition from a paraelectric to a near-rhombohedral vortex state at zero misfit strain with the decrease of temperature, complicated transformations of vortex domain patterns are found under nonzero misfit strain. Typically, orthorhombic, tetragonal and several unreported vortex domain patterns (*e.g.*, with zero toroidal moment) are found. Moreover, misfit strain-induced transformations into these domain patterns are also predicted for a ferroelectric nanodot with initial near-rhombohedral vortex state. Combining effects of the ambient temperature and misfit strain, a ''temperature-misfit strain'' phase-diagram depicting the fruitful vortex domain patterns of the nanodot was obtained. Our simulations indicate promising application of strain engineering in controlling the VDS in ferroelectric nanostructures.

1. Introduction

For their academic interests and important roles in domain and domain wall engineering, domain structures in ferroelectrics and multiferroics have undergone active investigation over several decades.[1] Particular examples are exotic domain patterns, including vertices, vortices, quadrupoles and other topological defects, which are manifested by singular polarization regions like polarization sources/sinks or polarization closures. These domain patterns are found to form in low-dimensional ferroelectric nanostructures or in multiferroics as a consequence of geometric confinement or the coupling of polarization to other order parameters.[2–17] While some technological challenges still remain in experimental preparation and characterization, prospective applications exploiting the functional properties and the small size of these domain patterns are attractive, such as developing high-density memory devices and novel functional devices.

Among these exotic domain patterns, novel toroidal polarization patterns consisting of closure domains, or vortex domain structures (VDSs), have garnered intensive attention recently. Belonging to a new kind of polarization ordering, *i.e.*, ferrotoroidicity, VDSs are believed to exhibit distinct characteristics and novel couplings with external fields, compared to the traditional ferroelectric domains. Up to now, the mechanisms of forming VDSs in various materials as well as the effects of factors, such as size, shape and boundary conditions, have been theoretically studied.[2–4,11,17] Meanwhile, experiments are also close to unambiguously characterizing and artificially creating nanoscale ferroelectric vortices.[5,7,8,14,15] Gaining regular control on VDSs is now an important issue for future applications, although there is still a long way to go.

In the literature, a number of theoretical works have focused on the characteristics of VDSs in low-dimensional ferroelectric nanostructures, especially when they are coupled with external fields, *e.g.*, electric or mechanical fields.[17–26] Particularly, using the effective Hamiltonian method, Ponomareva *et al.*[17] investigated the effect of electric boundary conditions and epitaxial

[a] *State Key Laboratory of Optoelectronic Materials and Technologies, School of Physics and Engineering, Sun Yat-sen University, 510275, Guangzhou, China. E-mail: zhengy35@mail.sysu.edu.cn, wangbiao@mail.sysu.edu.cn; Tel: +86 8411-3231*

[b] *Sino-French Institute of Nuclear Engineering and Technology, Zhuhai Campus, Sun Yat-sen University, Zhuhai, 519082, China*

[c] *School of optical and electronic information, Huazhong University of Science and Technology, Wuhan 430074, China*

strain on the dipole pattern of $Pb(Zr_{0.4}Ti_{0.6})O_3$ nanodots and wires. Prosandeev and Bellaiche[18] determined the characteristics and signatures of dipole vortices in ferroelectric nanodots through effective Hamiltonian simulations and analytical derivations. The characteristics of vortex switching, vortex rotation and vortex-to-polarization transformation induced by various electric fields in ferroelectric nanostructures were also investigated by effective Hamiltonian simulations and phase-field simulations.[19–24] While the above instructive works about controlling the vortex domain structures are mostly through electric means, it is also possible to gain regular control of the VDS through mechanical means. For example, Naumov and Bratkovsky[25] investigated the effects of misfit strain on the polarization patterns in flat perovskite nanoparticles and showed that equilibrium polarization patterns are strongly dependent on misfit strain. More recently, through phase-field simulations Chen *et al.*[26,27] also demonstrated that the vortex domain morphology in flat ferroelectric nanostructures, especially the size and number of vortices, can be regularly controlled by mechanical loads.

Nevertheless, compared with the wide and fruitful investigations on mechanical control of the conventional domain structures in ferroelectric thin films,[28–31] investigations focusing on mechanical control of VDSs are still scarce. Many issues remain to be further systematically investigated, such as the mechanical effect on the ground state of low-dimensional ferroelectric nanostructures, the response of a given vortex pattern to the mechanical fields, and the possibility of inducing transformations of various "vortex states" by mechanical fields, *etc.*

In this work, taking into account the inhomogeneous electromechanical fields, ambient temperature and surface effect, we report the effect of the misfit strains on the VDS of a $BaTiO_3$ nanodot. Based on the phase field model, effects of the misfit strains on the phase transition behavior of the nanodot, *i.e.*, transitions from paraelectric phase to ferroelectric/ferrotoroidic phase, as well as effects on the existing vortex domain patterns obtained at zero misfit strain of the nanodot, will be simulated and discussed. The temperature-misfit strain phase diagram for different vortex states will also be given. With the different vortex domain patterns meticulously classified, regularity of the misfit strain controlling the VDS of the nanodot will be demonstrated and discussed in depth.

2. Phase-field model

The simulated ferroelectric nanodot is assumed to be epitaxially grown on a rigid substrate as shown in Fig. 1(a). Due to the lattice mismatch between the ferroelectric dot and substrate, the nanodot undergoes misfit strains, *i.e.*, ε_{11}^{m}, ε_{12}^{m} and ε_{22}^{m}. According to the phase-field model, we consider as our thermodynamic reference a crystal of infinite extent (surfaceless) absent of applied fields, *i.e.*, electric, magnetic or mechanical (internal or external). The spontaneous polarization P is chosen as the order parameter to describe the domain pattern. Therefore, the electric displacement field D can be expressed as $D = \varepsilon_b E + P$, where E is the electric field and ε_b the background dielectric constant

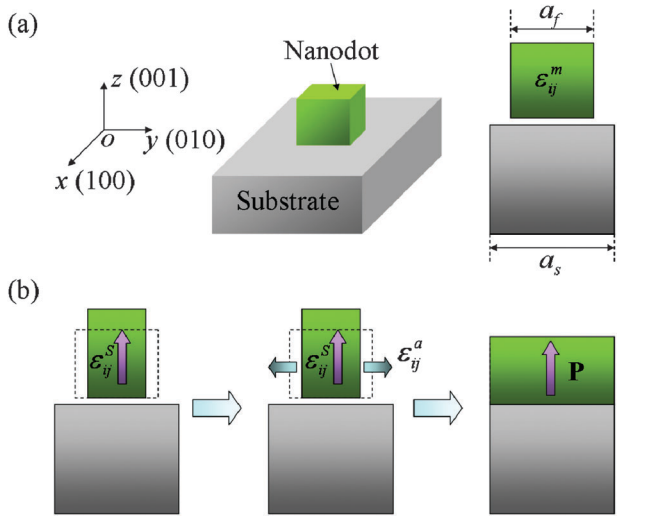

Fig. 1 Schematics of (a) the epitaxial nanodot grown on a rigid substrate and (b) a two-step strategy used to mimic the effect of the substrate.

tensor.[32–34] Since the background material is the paraelectric phase, which is in cubic crystal structure, the background dielectric constants in the three axis directions are the same, *i.e.*, $\varepsilon_b = \varepsilon_{11b} = \varepsilon_{22b} = \varepsilon_{33b}$.

Based on the phenomenological theory, the total free energy of the nanodot can be expressed as a function of polarization, spatial polarization gradients, mechanical strains and the electric field. It can be written as the sum of the Landau free energy F_{Land}, elastic energy F_{elas}, gradient energy F_{grad}, electrostatic energy F_{elec} and surface energy F_{surf}, *i.e.*,

$$\begin{aligned} F &= F_{Land} + F_{elas} + F_{grad} + F_{elec} + F_{surf} \\ &= \int_V (f_{Land} + f_{elas} + f_{grad} + f_{elec})\,dV + \int_S f_{surf}\,dS \end{aligned} \quad (1)$$

where f_{Land}, f_{elas}, f_{grad}, f_{elec} and f_{surf} are the corresponding free energy densities, V and S are the volume and surface of the nanodot.

For perovskite ferroelectrics, the Landau free energy density f_{Land} can be expressed for a zero-stress state up to an eight-order polynomial expansion as,[35–37]

$$\begin{aligned} f_{Land} = {} & a_1(P_1^2 + P_2^2 + P_3^2) + a_{11}(P_1^4 + P_2^4 + P_3^4) \\ & + a_{12}(P_1^2P_2^2 + P_2^2P_3^2 + P_1^2P_3^2) + a_{111}(P_1^6 + P_2^6 + P_3^6) \\ & + a_{112}[P_1^2(P_2^4 + P_3^4) + P_2^2(P_1^4 + P_3^4) + P_3^2(P_1^4 + P_2^4)] \\ & + a_{123}P_1^2P_2^2P_3^2 + a_{1111}(P_1^8 + P_2^8 + P_3^8) \\ & + a_{1112}[P_1^6(P_2^2 + P_3^2) + P_2^6(P_1^2 + P_3^2) + P_3^6(P_1^2 + P_2^2)] \\ & + a_{1122}(P_1^4P_2^4 + P_2^4P_3^4 + P_1^4P_3^4) \\ & + a_{1123}(P_1^4P_2^2P_3^2 + P_2^4P_1^2P_3^2 + P_3^4P_1^2P_2^2) \end{aligned} \quad (2)$$

where a_i, a_{ij}, a_{ijk} and a_{ijkl} are dielectric stiffness and higher order coefficients fitted to bulk properties and P_i is the ith component of polarization.

Ferroelectric phase transition involves structural changes and results in spontaneous strains. At zero-stress state, these strains

are called eigenstrains. For perovskite ferroelectrics, the eigenstrains can be expressed as,

$$\begin{aligned}\varepsilon_{11}^0 &= Q_{11}P_1^2 + Q_{12}\left(P_2^2 + P_3^2\right)\\ \varepsilon_{22}^0 &= Q_{11}P_2^2 + Q_{12}\left(P_3^2 + P_1^2\right)\\ \varepsilon_{33}^0 &= Q_{11}P_3^2 + Q_{12}\left(P_1^2 + P_2^2\right)\\ \varepsilon_{23}^0 &= Q_{44}P_2P_3\\ \varepsilon_{13}^0 &= Q_{44}P_1P_3\\ \varepsilon_{12}^0 &= Q_{44}P_1P_2\end{aligned} \tag{3}$$

where Q_{ij} is the electrostrictive coefficient.

Considering the epitaxial misfit strain and the incompatibility of the eigenstrains caused by the polarization, the elastic energy density of the ferroelectric nanodot is given by,

$$\begin{aligned}f_{\text{elas}} &= c_{ijkl}e_{ij}e_{kl} = c_{ijkl}\left(\varepsilon_{ij} - \varepsilon_{ij}^0\right)\left(\varepsilon_{kl} - \varepsilon_{kl}^0\right)\\ &= \frac{1}{2}C_{11}\left[\left(\varepsilon_{11} - \varepsilon_{11}^0\right)^2 + \left(\varepsilon_{22} - \varepsilon_{22}^0\right)^2 + \left(\varepsilon_{33} - \varepsilon_{33}^0\right)^2\right]\\ &\quad + C_{12}\left[\left(\varepsilon_{11} - \varepsilon_{11}^0\right)\left(\varepsilon_{33} - \varepsilon_{33}^0\right) + \left(\varepsilon_{22} - \varepsilon_{22}^0\right)\left(\varepsilon_{33} - \varepsilon_{33}^0\right)\right.\\ &\quad \left. + \left(\varepsilon_{11} - \varepsilon_{11}^0\right)\left(\varepsilon_{22} - \varepsilon_{22}^0\right)\right]\\ &\quad + 2C_{44}\left[\left(\varepsilon_{13} - \varepsilon_{13}^0\right)^2 + \left(\varepsilon_{23} - \varepsilon_{23}^0\right)^2 + \left(\varepsilon_{12} - \varepsilon_{12}^0\right)^2\right]\end{aligned} \tag{4}$$

where c_{ijkl} and C_{ij} are the four-order and reduced elastic coefficients, e_{ij} and ε_{ij} the elastic strains and total strains.

For simplicity, we assume the substrate is rigid without elastic relaxation, and the dimensions of the epitaxial nanodot are small compared with the substrate thickness. With this assumption, we can disregard the substrate, but mimic its effect by considering that the nanodot undergoes in-plane homogenous stresses, which keep the in-plane macroscopic shape deformations of the nanodot equal to the misfit strains, *i.e.*, $\varepsilon_{11}^{\text{m}}$, $\varepsilon_{12}^{\text{m}}$ and $\varepsilon_{22}^{\text{m}}$. Accordingly, a two-step strategy can be used to solve the final strain state of the epitaxial nanodot as in Fig. 1(b). (1) In the first step, the nanodot with polarization field is under a surface traction-free condition, except that its bottom surface is fixed in the z-direction due to the interfacial effect of a hard substrate. Inhomogeneous strain fields of the nanodot in this state, denoted as $\varepsilon_{ij}^{\text{S}}$, are determined by the mechanical equilibrium equation $c_{ijkl}(\varepsilon_{kl,j}^{\text{S}} - \varepsilon_{kl,j}^0)|_V = 0$ and corresponding mechanical boundary $u_3|_{z=0} = 0$. The macroscopic shape deformations of the nanodot in this state are the volume average of $\varepsilon_{ij}^{\text{S}}$, *i.e.*, $\bar{\varepsilon}_{ij}^{S} = \int_V \varepsilon_{ij}^{S}\mathrm{d}V$. (2) In the second step, external stresses are applied to the nanodot. The external stresses cause additional strains, *i.e.*, $\varepsilon_{ij}^{\text{a}}$, so as to keep the in-plane macroscopic shape deformations equal to the misfit strains, *i.e.*, $\bar{\varepsilon}_{11}^{\text{S}} + \varepsilon_{11}^{\text{a}} = \varepsilon_{11}^{\text{m}}$, $\bar{\varepsilon}_{22}^{\text{S}} + \varepsilon_{22}^{\text{a}} = \varepsilon_{22}^{\text{m}}$ and $\bar{\varepsilon}_{12}^{\text{S}} + \varepsilon_{12}^{\text{a}} = \varepsilon_{12}^{\text{m}}$. Additional strains along the z-direction are determined by the conditions $c_{i3kl}\varepsilon_{kl}^{\text{a}} = 0$. From this construction, we have the total strains of the nanodot as $\varepsilon_{ij} = \varepsilon_{ij}^{\text{S}} + \varepsilon_{ij}^{\text{a}}$.

The spatial polarization variation contributes a gradient energy to the total free energy. To the lowest order of the Taylor expansion, the gradient energy density of a perovskite ferroelectric takes the form of,

$$\begin{aligned}f_{\text{grad}} &= \frac{1}{2}G_{11}\left(P_{1,1}^2 + P_{2,2}^2 + P_{3,3}^2\right)\\ &\quad + G_{12}\left(P_{1,1}P_{2,2} + P_{2,2}P_{3,3} + P_{1,1}P_{3,3}\right)\\ &\quad + \frac{1}{2}G_{44}\left[\left(P_{1,2} + P_{2,1}\right)^2 + \left(P_{2,3} + P_{3,2}\right)^2 + \left(P_{1,3} + P_{3,1}\right)^2\right]\\ &\quad + \frac{1}{2}G'_{44}\left[\left(P_{1,2} - P_{2,1}\right)^2 + \left(P_{2,3} - P_{3,2}\right)^2 + \left(P_{1,3} - P_{3,1}\right)^2\right]\end{aligned} \tag{5}$$

with G_{11}, G_{12}, G_{44} and G'_{44} being the reduced gradient energy coefficients.

To take account of the polarization inhomogeneity across the surface due to surface truncation, an additional surface energy is introduced. Using the so-called extrapolation length δ_i^{eff},[38,39] the surface energy density of the ferroelectric nanodot can be approximately given by $f_{\text{surf}} = \frac{D_1^{\text{S}}P_2^2}{2\delta_1^{\text{eff}}} + \frac{D_2^{\text{S}}P_2^2}{2\delta_2^{\text{eff}}} + \frac{D_3^{\text{S}}P_3^2}{2\delta_3^{\text{eff}}}$, with D_i^{S} being the material coefficients related to the gradient energy coefficients and the surface orientation as $D_1^{\text{S}} = G_{11}n_1 + \left(G_{44} + G'_{44}\right)(n_2 + n_3)$, $D_2^{\text{S}} = G_{11}n_2 + \left(G_{44} + G'_{44}\right)(n_1 + n_3)$ and $D_3^{\text{S}} = G_{11}n_3 + \left(G_{44} + G'_{44}\right)(n_1 + n_2)$, where n_i are the components of the normal unit vector of the surface.

In the absence of an external electric field, the total electric field is equal to depolarization field induced by spatial polarization variation and incomplete screening of the polarization charges at truncated surfaces. According to previous works,[23,32,40] the electric energy density of a given polarization distribution is written as $f_{\text{elec}} = -P_1E_1 - P_2E_2 - P_3E_3 - \frac{1}{2}\varepsilon_{\text{b}}(E_1E_1 + E_2E_2 + E_3E_3)$. Under the open-circuit condition, for a free-charge-absent body the depolarization field can be calculated by the electrostatic equilibrium equation $D_{i,i}|_V = 0$ and the corresponding boundary condition $D_in_i|_S = 0$, with n_i being the ith component of the unit vector normal to the surface.

Integrating the free energy densities over the entire volume and surfaces, yields the total free energy of the nanodot. In the following, the mechanical strains and electric field are treated in an adiabatic way during the polarization evolution, under the assumption that mechanical and electric equilibrium can be instantaneously reached once the spontaneous polarization distribution is set down. The temporal evolution of the spontaneous polarization field is then described by the time-dependent Ginzburg–Landau (TDGL) equations, *i.e.*,

$$\frac{\partial P_i}{\partial t} = -M\frac{\delta F}{\delta P_i}, \quad (i = 1, 2, 3) \tag{6}$$

where M is the kinetic coefficient and t is time.

3. Results and discussions

In the following, we consider cubic $BaTiO_3$ nanodots (001) epitaxially grown on cubic substrates (001). In this case, the nanodots undergo biaxially equal misfit strains, *i.e.*, $\varepsilon_{11}^{\text{m}} = \varepsilon_{22}^{\text{m}} = u_{\text{m}}$ and $\varepsilon_{12}^{\text{m}} = 0$.

Furthermore, the surfaces of the nanodots are traction free, except for the bottom surface being fixed in the z-direction due to the interfacial effect of a hard substrate. An open-circuit electric boundary condition is adopted to obtain a strong vortex effect. The simulated nanodots are divided into three-dimensional $n \times n \times n$ elements at a scale of $\Delta x = \Delta y = \Delta z = 0.4$ nm. The polarization evolution is solved numerically by discretizing the TDGL equation in time. The time step is chosen to be $\Delta t = 0.01 a_0 M$, where $a_0 = |a_1|_{T=300\mathrm{K}}$. At each time step, the mechanical strains and electric field are obtained by solving the mechanical and electrostatic equilibrium equations with appropriate boundary conditions using the finite element method. Values of the expansion coefficients of the Landau potential, the elastic compliances, the electrostrictive coefficients and the gradient coefficients,[41] the extrapolation length,[39] and the background dielectric constant[32,33] in calculations are listed in SI units as follows, $a_1 = 4.124(T - 388) \times 10^5$, $a_{11} = -2.097 \times 10^8$, $a_{12} = 7.974 \times 10^8$, $a_{111} = 1.294 \times 10^9$, $a_{112} = -1.950 \times 10^9$, $a_{123} = -2.5009 \times 10^9$, $a_{1111} = 3.863 \times 10^{10}$, $a_{1112} = 2.529 \times 10^{10}$, $a_{1122} = 1.637 \times 10^{10}$, $a_{1123} = 1.367 \times 10^{10}$, $C_{11} = 27.5 \times 10^{10}$, $C_{12} = 17.9 \times 10^{10}$, $C_{44} = 5.43 \times 10^{10}$, $Q_{11} = 0.11$, $Q_{12} = -0.045$, $Q_{44} = 0.029$, $\delta_i^{\mathrm{eff}} \approx 4.3 \times 10^{-8}$, $\varepsilon_b = 4.425 \times 10^{-10}$, $G_{11} = 5.1 \times 10^{-10}$, $G_{12} = 0$, $G_{44} = G'_{44} = 1 \times 10^{-11}$. Here we use anisotropic gradient coefficients to give a better description of the 90° domain wall of $BaTiO_3$. A series of simulations on $8 \times 8 \times 8$, $10 \times 10 \times 10$ and $12 \times 12 \times 12$ nanodots have been conducted. The results found are similar for nanodots of all three sizes, therefore in the following we mainly present those of the $8 \times 8 \times 8$ nanodot.

3.1. The domain pattern of nanodots cooled down at zero misfit strain

We start our investigation on the domain pattern of nanodots under zero misfit strain, *i.e.*, $u_m = 0$. To obtain the ground state of the domain pattern, the nanodots are simulated to cool down from a high temperature in the paraelectric region by a step of 5 K. A random polarization perturbation is used to initiate the simulation, and it was used as the initial domain pattern for the next temperature step until the stable domain pattern was not paraelectric. At each temperature, the stable domain pattern is obtained by equilibrating the system for a sufficiently long time.

Simulated results of the domain pattern evolution of nanodots with different sizes are depicted in Fig. 2. As shown in Fig. 2(a), the toroidal moment is adopted to characterize the vortex domain pattern, *i.e.*, $\boldsymbol{g} = \frac{1}{V}\int_V \boldsymbol{r} \times (\boldsymbol{P} - \bar{\boldsymbol{P}})\mathrm{d}V$, with V being the volume of the system, $\boldsymbol{r}$ the position vector, and $\bar{\boldsymbol{P}}$ the average polarization of the system. Fig. 2(b) also depicts the domain morphologies of a $10 \times 10 \times 10$ nanodot at selected temperatures. (Note that in the following figures, all the domain patterns are plotted with the same color bar as the one in Fig. 2(b)) It can be seen that the nanodots indeed undergo paraelectric-to-ferrotoroidic transition. The phase transition temperature for the $8 \times 8 \times 8$, $10 \times 10 \times 10$ and $12 \times 12 \times 12$ nanodots is about 240 K, 270 K and 285 K, respectively,

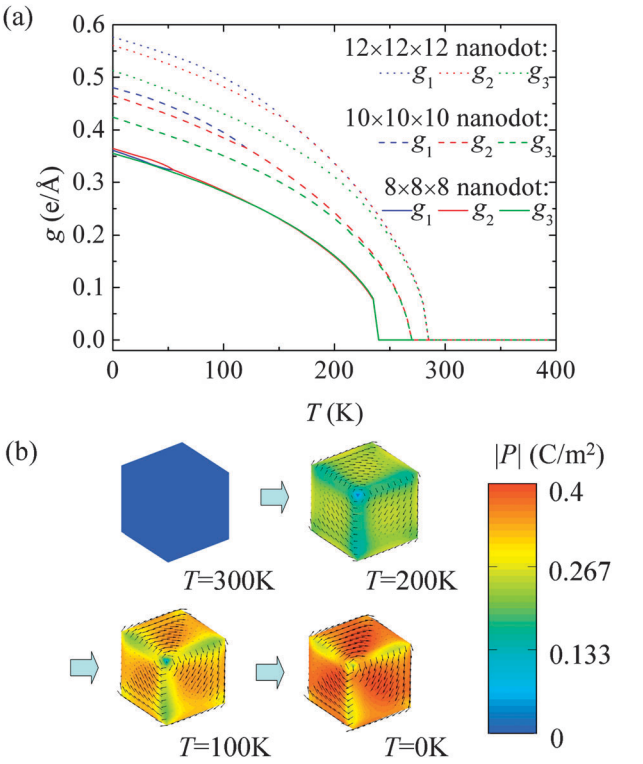

Fig. 2 Simulated results of the domain pattern evolution of nanodots under zero misfit strain in a cooling process. (a) The temperature dependence of the toroidal moment and (b) the domain morphologies of a $10 \times 10 \times 10$ nanodot at selected temperatures.

which increases as the nanodot size increases. Nevertheless, due to the small size of the nanodots, the transition temperatures are much lower than the Curie temperature of the bulk material, *i.e.*, $T_c = 388$ K. Below the transition temperature, the nanodots adopt a near-rhombohedral vortex domain pattern (*i.e.*, $g_1 \approx g_2 \approx g_3$) with the vortex axis almost parallel to the (111) direction. Note that the effect of substrate precludes the forming of perfect rhombohedral vortex domain pattern (*i.e.*, $g_1 = g_2 = g_3$) that is observed in free-standing $BaTiO_3$ nanodots.[18] Nevertheless, this effect is rather small for zero misfit-strain, and the single transition from paraelectric to the near-rhombohedral vortex domain pattern during the whole cooling process is quite similar to that observed in free-standing nanodots.

3.2. The domain pattern of a nanodot cooled at nonzero misfit strain

It can be seen from the above that the domain pattern of the nanodots remains a near-rhombohedral vortex domain pattern during cooling at zero misfit strain. To see the effect of misfit strain on the evolution of the domain pattern in a nanodot when the temperature decreases from the paraelectric region, in this section we conduct simulations similar with the previous section but with nonzero misfit strain on an $8 \times 8 \times 8$ nanodot. To clearly characterize the domain patterns, in the following we generally analyze each domain pattern through

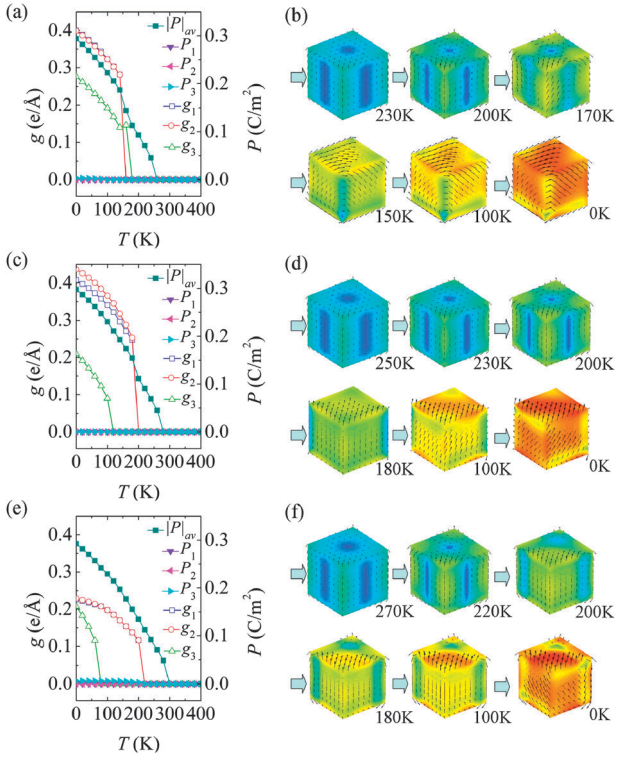

Fig. 3 Simulated results of the domain pattern evolution of a nanodot under small compressive strain in a cooling process. (a) and (b) $u_m = -0.001$, (c) and (d) $u_m = -0.002$, and (e) and (f) $u_m = -0.003$.

plotting its morphologies and calculating the components of the toroidal moment and the polarization vector, together with the mean magnitude of polarization, $|P|_{av} \equiv \int_V \sqrt{P_1^2 + P_2^2 + P_3^2}\,dV$. For all the simulations, the obtained domain patterns are found to be nonpolar or near nonpolar, *i.e.*, $P_1 \approx P_2 \approx P_3 \approx 0$.

3.2.1. Compressive misfit strain. For small compressive strains, *i.e.*, $u_m = -0.001$, $u_m = -0.002$, and $u_m = -0.003$, the simulated results are shown in Fig. 3(a) and (b), (c) and (d), and (e) and (f), respectively. The results show that the phase transition behavior of the ferroelectric nanodot in a cooling process under compressive strain is quite different from that at zero-misfit strain as shown in Fig. 2. In general, as the temperature decreases from the paraelectric region, the nanodot would at first adopt a highly symmetrical multi-vortex domain pattern rather than the near-rhombohedral vortex domain pattern. This domain pattern consists of four vortices with their toroidal axes along the $(\bar{1}00)$, (100), $(0\bar{1}0)$, and (100) directions respectively, with the polarization dipoles mainly along the *z*-axis. By tracing the evolution of the toroidal moment and the mean magnitude of polarization as shown in Fig. 3(a), (c) and (e), it can be found that the highly symmetrical multi-vortex domain pattern has zero toroidal moment. It is easy to see that this configuration can largely decrease the coupling energy between the polarization and the compressive strain. As the temperature further decreases, the highly symmetrical multi-vortex domain pattern is not stable. Particularly, for $u_m = -0.001$, the domain pattern would change into a similar pattern but with tilted vortices (*e.g.* $T = 200$ K in Fig. 3(b)). This domain pattern has a nonzero toroidal moment as $g_1 = g_2 = 0$, $g_3 \neq 0$ and is only stable for a narrow temperature range. At lower temperatures it would destabilize into a single vortex state with its toroidal moment becoming $g_1 \approx g_2 \neq 0$, $g_3 \neq 0$ (*e.g.* $T = 150$ K in Fig. 3(b)). For $u_m = -0.002$, the highly symmetrical multi-vortex domain pattern would directly destabilize into a single-vortex state at about 180 K (see Fig. 3(d)). Such a single-vortex state is orthorhombic (*i.e.* $g_1 \approx g_2 \neq 0$, $g_3 = 0$) in the high temperature range, and becomes near-rhombohedral (*i.e.* $g_1 \approx g_2 \neq 0$, $g_3 \neq 0$) at low temperatures. For $u_m = -0.003$, as temperature decreases, the domain pattern remains in a multi-vortex state, but with two large and two small vortices (*e.g.* $T = 200$ K in Fig. 3(f)). Similar to the case of $u_m = -0.002$, we subsequently obtain $g_1 = g_2 = g_3 = 0$, $g_1 \approx g_2 \neq 0$, $g_3 = 0$ and $g_1 \approx g_2 \neq 0$, $g_3 \neq 0$ as the temperature decreases.

To see the effect of a large compressive misfit strain, we further simulated the cooling-down domain pattern of a nanodot under misfit strains ranging from -0.02 to -0.01. The results show that the effects of the misfit strain in this range are similar, but quite different from those of small compressive misfit strains as shown in Fig. 3. The simulated temperature dependencies of the toroidal moment, the polarization vector and the mean magnitude of polarization for $u_m = -0.01$ and $u_m = -0.015$ are depicted in Fig. 4(a) and (b), respectively. The simulated domain pattern at selected temperatures for $u_m = -0.015$ is also shown in Fig. 4(c). From these results, it can be seen that due to the large misfit strain, the transition temperature of the nanodot increases significantly (~550 K and ~790 K for $u_m = -0.01$ and $u_m = -0.015$, respectively).

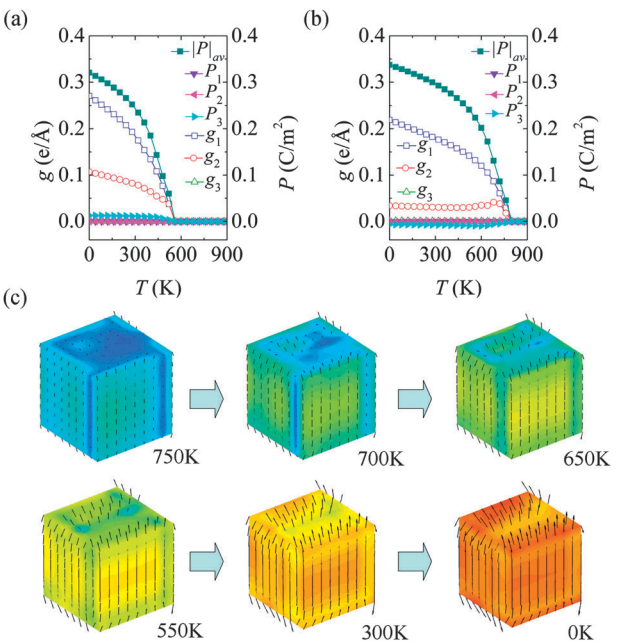

Fig. 4 Simulated results of the domain pattern evolution of a nanodot under a large compressive strain in a cooling process. Temperature dependence of the toroidal moment and polarization at (a) $u_m = -0.001$ and (b) $u_m = -0.015$. (c) The domain morphologies at selected temperatures for $u_m = -0.015$.

Moreover, the nanodot kept adopting a stripe-like domain pattern with $g_1 \neq 0$, $g_2 \neq 0$, $g_3 = 0$ and the polarization dipoles mainly aligned along the z-direction.

3.2.2. Tensile misfit strain. From the previous section, we can see that compressive misfit strain tends to align the polarization dipoles along the z-direction and thus results in domain patterns with a small z-component of the toroidal moment, such as the highly symmetrical multi-vortex domain pattern and the orthorhombic vortex domain pattern. It is also possible to align the polarization dipoles along the x–y plane by applying tensile strain, which results in domain patterns with a large z-component of the toroidal moment, such as a tetragonal vortex domain pattern (*i.e.* $g_1 = g_2 = 0$, $g_3 \neq 0$). This can be seen in Fig. 5, which depicts the simulated phase transition behavior of a nanodot under small tensile misfit strains during a cooling process. In particular, Fig. 5(a) and (b), (c) and (d) and (e) and (f) respectively depict the evolution of the domain pattern in a nanodot under tensile misfit strain $u_m = 0.001$, $u_m = 0.002$, and $u_m = 0.003$. Unlike the multiple behaviors shown in small compressive misfit strains (see Fig. 3), results show that the transition behaviors of the nanodot are similar for the small tensile misfit strains. In general, the nanodot undergoes a phase transition from paraelectric to a tetragonal vortex state (*i.e.* $g_1 = g_2 = 0$, $g_3 \neq 0$) as temperature decreases. With temperature further decreasing, the tetragonal vortex state becomes unstable and destabilizes into a new domain pattern with its toroidal moment being $g_1 = g_2 \neq 0$, $g_3 \neq 0$. We found

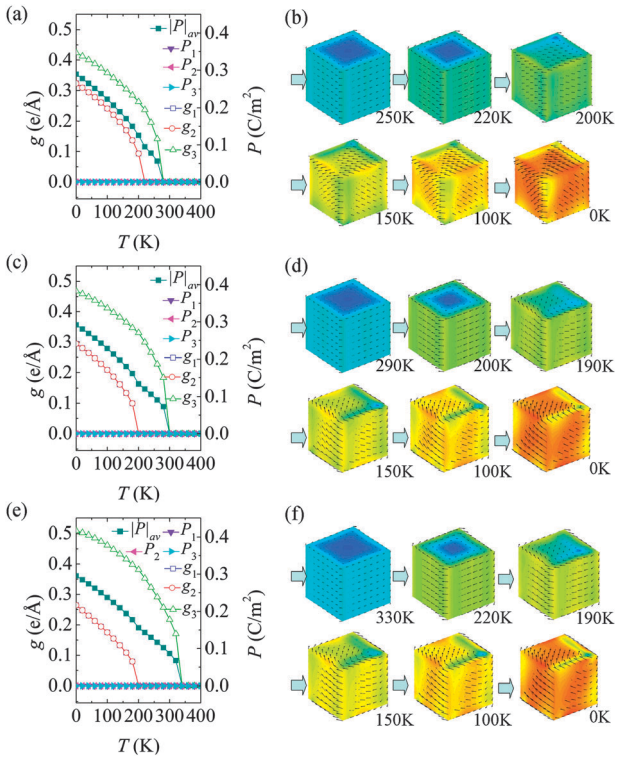

Fig. 5 Simulated results of the domain pattern evolution of a nanodot under small tensile strain in a cooling process. (a) and (b) $u_m = 0.001$, (c) and (d) $u_m = 0.002$, and (e) and (f) $u_m = 0.003$.

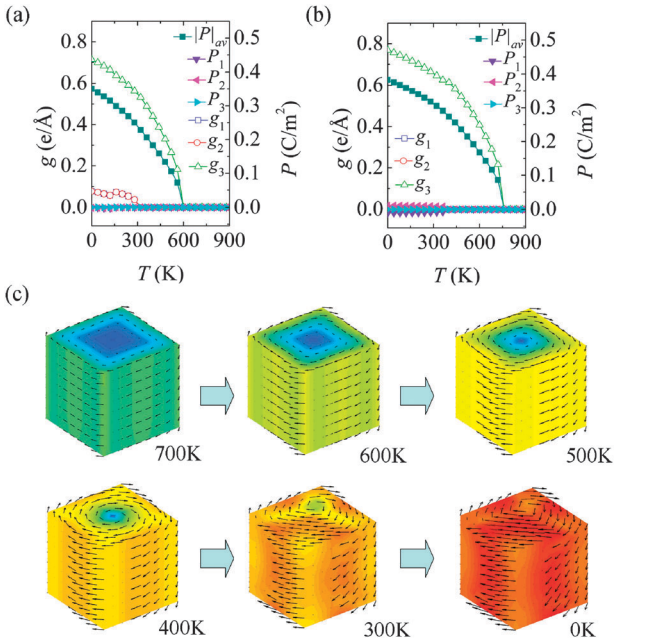

Fig. 6 Simulated results of the domain pattern evolution of a nanodot under large tensile strain in a cooling process. Temperature dependence of the toroidal moment and polarization at (a) $u_m = 0.01$ and (b) $u_m = 0.015$. (c) The domain morphologies at selected temperatures for $u_m = 0.015$.

that the polarization dipoles of this domain pattern are also mainly confined in the x–y plane as those of the tetragonal vortex state. Nevertheless, the toroidal center of each dipole vortex plane tends to depart from its geometric center. This domain pattern seems to be a result of the competing tendencies of being rhombohedral and being tetragonal. Comparing Fig. 5(a), (c) and (e), it can be also noted that the existing temperature range of the tetragonal domain pattern becomes larger as the tensile misfit strain increases.

The effect of large tensile misfit strain on the cooled-down domain patterns of a nanodot was also investigated. The typical results for a nanodot under $u_m = 0.01$ and $u_m = 0.015$ are shown in Fig. 6. The evolution of the domain pattern at large tensile misfit strains are quite similar to those of small tensile misfit strains as shown in Fig. 5. As temperature decreases, a transition from paraelectric to a tetragonal vortex state is generally observed, and at lower temperatures the tetragonal domain pattern would also transform into the domain pattern with $g_1 = g_2 \neq 0$, $g_3 \neq 0$. Nevertheless, due to the large misfit strain, the transition temperature increases significantly ($\sim$580 K and $\sim$750 K for $u_m = 0.01$ and $u_m = 0.015$, respectively). Moreover, the in-plane components of the toroidal moment of the low temperature domain pattern are significantly depressed as the tensile misfit strain increases.

3.3. The misfit strain effect on a nanodot with initial vortex domain patterns

So far, we have shown that misfit strain can significantly affect the phase transition behavior of the nanodot from paraelectric as temperature decreases. It is also practically important to see

whether misfit strain can bring about significant change on the formed vortex domain pattern of the nanodot. To achieve this, the nanodot was further simulated under misfit strains ranging from −0.02 to 0.02, with initial vortex domain patterns being those obtained at zero misfit strain. From our study, the following observations can be made. (a) Similar to the previous results, compressive misfit strain tends to align the dipoles along the *z*-axis while the tensile strain tends to align the dipoles along the in-plane directions. (b) Consequently, misfit strain induces the rotation of the dipole vortex as well as transformations to new domain patterns. (c) The *z*-component of the toroidal moment tends to increase under compressive misfit strain and decrease under tensile strain, while the other two components show a contrary behavior. Furthermore, abrupt or abnormal changes may happen, due to new patterns appearing. (d) The misfit strain effect on the vortex domain pattern is a strong function of temperature. At relatively low temperatures, misfit strain affects the domain pattern smoothly and mainly induces the rotation of the dipole vortex. At relatively high temperatures, the effect of misfit strain is more fruitful and induces more domain patterns. (e) Although the misfit strain changes from −0.02 to 0.02, the polarization vector components remain near zero, whereas the toroidal moment and the mean magnitude of polarization change significantly, indicating that no polar domain pattern is formed.

These observations can be found in the representative results at T = 50 K, 220 K and 250 K, as depicted in Fig. 7(a) and (b), (c) and (d) and (e) and (f), respectively. (Note that at T = 250 K, the nanodot is near-paraelectric with a negligible polarization magnitude.)

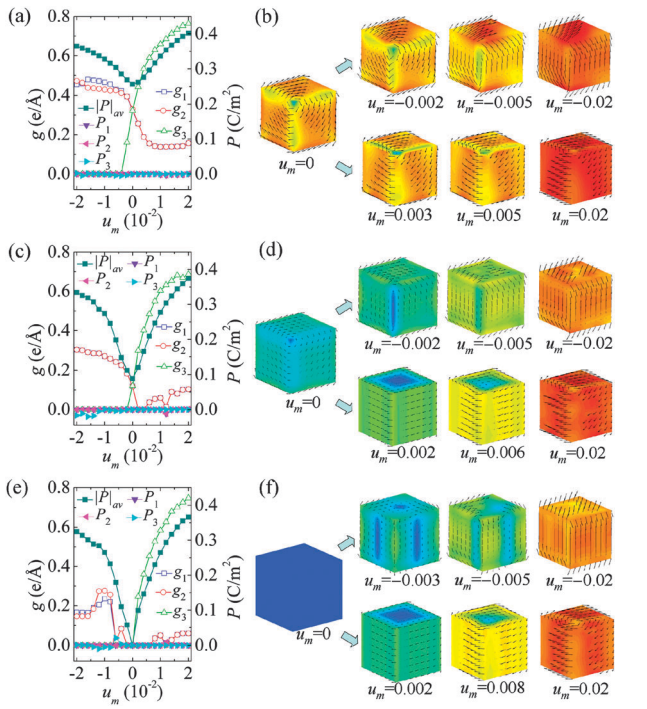

Fig. 7 Simulated results of the misfit strain effect on a nanodot with initial vortex domain patterns obtained at zero misfit strain at (a) and (b) T = 50 K, (c) and (d) T = 220 K and (e) and (f) T = 250 K.

It can be seen that the components of the toroidal moment, the mean magnitude of polarization and the domain pattern are a strong function of misfit strain at all temperatures, which clearly demonstrate the effective control of misfit strain on the vortex domain pattern of the nanodot. A particularly exciting indication is that misfit strain can rotate the dipole vortex and induce transformations from the initial VDS into other vortex domain patterns. For example in Fig. 7(a) and (b), results show that at T = 50 K the axis of the initial near-rhombohedral vortex domain pattern rotates to a ⟨110⟩ direction and transforms into an orthorhombic one (*i.e.* $g_1 = g_2 \neq 0$, $g_3 = 0$) as compressive misfit strain increases. Whereas it prefers to align along the *z*-direction under tensile misfit strain, with g_z increasing significantly. Similar results are found at T = 220 K as shown in Fig. 7(c) and (d), yet the vortex domain pattern becomes tetragonal (*i.e.* $g_1 = g_2 = 0$, $g_3 \neq 0$) at small tensile misfit strains, *i.e.* $0.002 \leq u_m \leq 0.004$. Interestingly, at T = 250 K new vortex patterns with zero toroidal moment, *i.e.* $g_1 = g_2 = g_3 = 0$, are found under compressive misfit strain (see Fig. 7(e) and (f)). Moreover, the vortex pattern of the nanodot at large compressive misfit strains becomes stripe-like (*e.g.* $u_m = -0.02$ for T = 220 K and 250 K as respectively shown in Fig. 7(d) and (f)).

To clearly see the effect of misfit strain on the vortex domain pattern, we further classify the different vortex domain patterns and draw a "temperature-misfit strain" phase-diagram depicting the vortex domain pattern as shown in Fig. 8. It must be pointed out that the classification is a rather rough one. Nevertheless, several distinct domain patterns are picked out, which have been denoted by different symbols and plotted in Fig. 8. It can be seen that compressive misfit strain tends to transform the initial near-rhombohedral (solid star) or near-paraelectric (hollow star) domain pattern, into vortex domain patterns favoring *z*-directional dipoles. These domain patterns include the orthorhombic vortex state (solid diamond), the one with stripe-like domains inside the nanodot (hollow diamond) and the highly symmetrical multi-vortex domain pattern with zero toroidal moment (solid circle and hollow circle). Meanwhile, for tensile misfit strain, the initial vortex domain patterns tend to transform into domain patterns with dipoles lying in the *x*–*y* plane, *i.e.* the tetragonal one (hollow triangle) and the one with the toroidal center of the dipole vortex plane, tend to depart from its geometric center (solid triangle). For both compressive and tensile misfit strain, relatively higher temperatures bring more fruitful domain patterns.

Finally, we would like to point out that the appearance of fruitful vortex domain patterns originate from the various roles of the free energy components of the system. Particularly, electrostatic energy is responsible for the appearance of dipole vortices. Elastic energy mainly controls the orientation of the dipole vortex. Landau free energy plays an important role in the formation of the near-rhombohedral vortex and the tilting of dipole vortex at low temperatures. Gradient energy is important in the complexity of the domain pattern, *e.g.* a single vortex or multi-vortices. Surface energy mainly affects the phase transition temperature. More importantly, these free energy components together determine the domain pattern of the nanostructure in

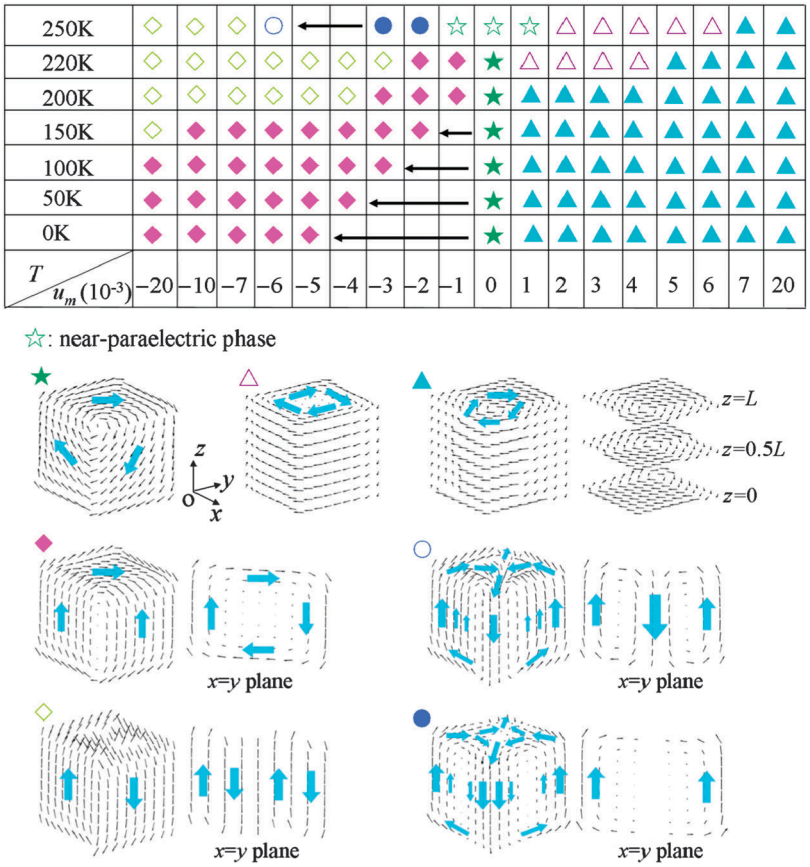

Fig. 8 Equilibrium vortex domain pattern as a function of misfit strain and temperature for a nanodot with initial vortex domain patterns obtained at zero misfit strain. Various domain patterns are denoted by different symbols. The arrows in the table indicate the domain patterns are in between those at either side.

a comprehensive way, which is demonstrated to be complicated and fruitful. In our investigation, we mainly investigated the effects of elastic energy and Landau free energy through adjusting misfit strain and temperature, fruitful results can also be achieved by mainly affecting other free energy components, such as the electrostatic energy.[42]

4. Summary and conclusions

In summary, fruitful vortex domain patterns in ferroelectric nanodots controlled by the misfit strain are predicted using phase-field simulation. It is shown that the ferroelectric nanodot adopts a single phase transition from paraelectric phase to a near-rhombohedral vortex state at zero misfit strain as temperature decreases. Meanwhile, the misfit strain can induce much complicated phase transition behaviors for the vortex domain states of the nanodot. Our calculations found that the orthorhombic, tetragonal and several unreported vortex domain patterns (*e.g.* with zero toroidal moment) can stably form. More importantly, a temperature-misfit strain phase diagram has been given, which also depicts the fruitful vortex domain patterns of ferroelectric nanodots. To the best of our knowledge, these new vortex domain patterns and the misfit strain-induced transformations between vortex domain patterns have not been reported for ferroelectric nanodots yet. Our investigations should be meaningful to further reveal the different properties of these domain patterns, and the simulations should give an important indication of the potential application of controlling the VDS in ferroelectric nanostructures by mechanical means.

Acknowledgements

The authors acknowledge the financial support of the National Natural Science Foundation of China (NSFC) (no. 10902128, 10732100, 50802026, 10972239). Yue Zheng also thanks support from the Fundamental Research Funds for the Central Universities, New Century Excellent Talents in University, Research Fund for the Doctoral Program of Higher Education, Fok Ying Tung Foundation, Science and Technology Innovation Project of Guangdong Provincial Education Department and Guangdong Natural Science Funds for Distinguished Young Scholar.

References

1 G. Catalan, J. Seidel, R. Ramesh and J. F. Scott, *Rev. Mod. Phys.*, 2012, **84**, 119–156.
2 H. Fu and L. Bellaiche, *Phys. Rev. Lett.*, 2003, **91**, 257601.
3 I. I. Naumov, L. Bellaiche and H. Fu, *Nature*, 2004, **432**, 737–740.

4 S. Prosandeev, I. Ponomareva, I. Naumov, I. Kornev and L. Bellaiche, *J. Phys.: Condens. Matter*, 2008, **20**, 193201.
5 A. Gruverman, D. Wu, H.-J. Fan, I. Vrejoiu, M. Alexe, R. J. Harrison and J. F. Scott, *J. Phys.: Condens. Matter*, 2008, **20**, 342201.
6 A. Schilling, D. Byrne, G. Catalan, K. G. Webber, Y. A. Genenko, G. S. Wu, J. F. Scott and J. M. Gregg, *Nano Lett.*, 2009, **9**, 3359–3364.
7 B. J. Rodriguez, X. S. Gao, L. F. Liu, W. Lee, I. I. Naumov, A. M. Bratkovsky, D. Hesse and M. Alexe, *Nano Lett.*, 2009, **9**, 1127–1131.
8 N. Balke, S. Choudhury, S. Jesse, M. Huijben, Y. H. Chu, A. P. Baddorf, L. Q. Chen, R. Ramesh and S. V. Kalinin, *Nat. Nanotechnol.*, 2009, **4**, 868–875.
9 Y. Ivry, D. P. Chu, J. F. Scott and C. Durkan, *Phys. Rev. Lett.*, 2010, **104**, 207602.
10 L. J. McGilly, A. Schilling and J. M Gregg, *Nano Lett.*, 2010, **10**, 4200–4205.
11 M. G. Stachiotti and M. Sepliarsky, *Phys. Rev. Lett.*, 2011, **106**, 137601.
12 C. T. Nelson, B. Winchester, Y. Zhang, S.-J. Kim, A. Melville, C. Adamo, C. M. Folkman, S.-H. Baek, C.-B. Eom, D. G. Schlom, L.-Q. Chen and X. Pan, *Nano Lett.*, 2011, **11**, 828–834.
13 L. J. McGilly and J. M. Gregg, *Nano Lett.*, 2011, **11**, 4490–4495.
14 R. G. P. McQuaid, L. J. McGilly, P. Sharma, A. Gruverman and J. M. Gregg, *Nat. Commun.*, 2011, **2**, 404.
15 C.-L. Jia, K. W. Urban, M. Alexe, D. Hesse and I. Vrejoiu, *Science*, 2011, **331**, 1420–1423.
16 A. Schilling, S. Prosandeev, R. G. P. McQuaid, L. Bellaiche, J. F. Scott and J. M. Gregg, *Phys. Rev. B: Condens. Matter Mater. Phys.*, 2011, **84**, 064110.
17 I. Ponomareva, I. Naumov and L. Bellaiche, *Phys. Rev. B: Condens. Matter Mater. Phys.*, 2005, **72**, 214118.
18 S. Prosandeev and L. Bellaiche, *Phys. Rev. B: Condens. Matter Mater. Phys.*, 2007, **75**, 094102.
19 S. Prosandeev, I. Ponomareva, I. Kornev, I. Naumov and L. Bellaiche, *Phys. Rev. Lett.*, 2006, **96**, 237601.
20 I. Naumov and H. Fu, *Phys. Rev. Lett.*, 2007, **98**, 077603.
21 S. Prosandeev, I. Ponomareva, I. Kornev and L. Bellaiche, *Phys. Rev. Lett.*, 2008, **100**, 047201.
22 S. Prosandeev and L. Bellaiche, *Phys. Rev. Lett.*, 2008, **101**, 097203.
23 I. Naumov and H. Fu, *Phys. Rev. Lett.*, 2008, **101**, 197601.
24 J. Wang, *Appl. Phys. Lett.*, 2010, **97**, 192901.
25 I. Naumov and A. M. Bratkovsky, *Phys. Rev. Lett.*, 2008, **101**, 107601.
26 W. J. Chen, Y. Zheng and B. Wang, *Appl. Phys. Lett.*, 2012, **100**, 062901.
27 W. J. Chen, Y. Zheng and B. Wang, *Sci. Rep.*, 2012, **2**, 796.
28 N. A. Pertsev, A. G. Zembilgotov and A. K. Tagantsev, *Phys. Rev. Lett.*, 1998, **80**, 1988.
29 V. G. Kukhar, N. A. Pertsev, H. Kohlstedt and R. Waser, *Phys. Rev. B: Condens. Matter Mater. Phys.*, 2006, **73**, 214103.
30 Y. L. Li, S. Y. Hu, Z. K. Liu and L. Q. Chen, *Appl. Phys. Lett.*, 2001, **78**, 3878.
31 S. Y. Hu, Y. L. Li and L. Q. Chen, *J. Appl. Phys.*, 2003, **94**, 2542.
32 C. H. Woo and Y. Zheng, *Appl. Phys. A: Mater. Sci. Process.*, 2008, **91**, 59–63.
33 Y. Zheng and C. H. Woo, *Appl. Phys. A: Mater. Sci. Process.*, 2009, **97**, 617–626.
34 A. K. Tagantsev, *Ferroelectrics*, 2008, **375**, 19–27.
35 M. J. Haun, E. Furman, S. J. Jang, H. A. McKinstry and L. E. Cross, *J. Appl. Phys.*, 1987, **62**, 3331.
36 Y. L. Li and L. Q. Chen, *Appl. Phys. Lett.*, 2006, **88**, 072905.
37 Y. L. Wang, A. K. Tagantsev, D. Damjanovic, N. Setter, V. K. Yarmarkin and A. I. Sokolov, *Phys. Rev. B: Condens. Matter Mater. Phys.*, 2006, **73**, 132103.
38 R. Kretschmer and K. Binder, *Phys. Rev. B: Condens. Matter Mater. Phys.*, 1979, **20**, 1065.
39 K. Ishikawa and T. Uemori, *Phys. Rev. B: Condens. Matter Mater. Phys.*, 1999, **60**, 11841.
40 L. D. Landau, E. M. Lifshitz and L. P. Pitaevskii, *Electrodynamics of continuous media*, Oxford University Press, Oxford, 1984.
41 J. Hlinka and P. Márton, *Phys. Rev. B: Condens. Matter Mater. Phys.*, 2006, **74**, 104104.
42 C. M. Wu, W. J. Chen, D. C. Ma, C. H. Woo and Y. Zheng, *J. Appl. Phys.*, 2012, **112**, 104108.